

Accumulation of particles in propagating fronts

Karl R. Helfrich

Department of Physical Oceanography, Woods Hole Oceanographic Institution, Woods Hole, Massachusetts 02543

Jesús Pineda

Biology Department, Woods Hole Oceanographic Institution, Woods Hole, Massachusetts 02543

Abstract

Field observations imply that accumulation and advection of invertebrate larvae and other plankton by propagating fronts provides an efficient mechanism for the cross-shelf transport and subsequent coastal settlement of larvae and plankton. Gravity currents propagating into a heavier, uniform-density fluid are known to have near-surface velocities u that exceed the propagation speed c of the gravity current nose. It is shown by simple dam-break laboratory experiments and through corresponding numerical solutions of two-dimensional stratified flow and Lagrangian particle advection that this characteristic of gravity currents can lead to accumulation in the gravity current nose of particles that originate well behind the gravity current head. However, efficient particle accumulation and transport with the speed c only occurs for particles with sufficient vertical buoyancy or vertical swimming capability. Weakly buoyant or neutral particles are swept down and back away from the gravity current head by the circulation in this region. A dam break into an ambient fluid with stratification (two-layered) could result in the transport of some particles that are initially trapped in the forepart of the leading disturbance, an undular bore. However, this situation does not result in significant accumulation of particles at the leading edge of the disturbance. The numerical solutions show that particles that originate in the dense fluid ahead of the gravity current are much less likely to be accumulated at the gravity current nose. A simple scaling criterion for the minimum vertical buoyancy velocity for efficient accumulation and transport of buoyant particles based on the gravity current and particle characteristics is developed and compares favorably with the numerical results. The implications of these results for transport of larvae in coastal environments are discussed.

The dynamics of marine benthic invertebrate populations are greatly affected by larval transport. For near-shore populations, larval transport prior to settlement includes at least three processes: cross-shore advection, because larvae are generally very small and cannot control their cross-shore position by swimming alone; larval behavior, because by swimming vertically, larvae might be able to exploit some depth-dependent cross-shore flows; and accumulation by convergent circulation in propagating features, because cross-shore advection of larvae is often dependent on the retention of larvae at the propagating features.

Several hypotheses of onshore larval transport, namely surface slicks over linear internal waves (Shanks 1983), internal bore warm fronts (Pineda 1994), and upwelling relaxation fronts (Farrell et al. 1991), invoke concentration of larvae at propagating features. These hypotheses state that larvae become concentrated at convergent features aligned parallel to the coastline and that larval transport occurs as these linear features propagate shoreward.

The interplay between transport and accumulation is poorly understood; issues include (1) the dependency of transport on accumulation, and of accumulation on larval behavior, and (2) whether the frontal larvae originate onshore or off-

shore of the propagating front. The first issues are important because if there were a dependency of transport on accumulation and of accumulation on behavior, only taxa with certain behaviors would be transported. Second, different taxa can have different distributions onshore and offshore of the propagating features, with larvae sometimes occurring predominantly only on one side. Here, frontal accumulation would depend on the interplay between the structure of the flow around the fronts and the horizontal distribution of the larvae (*see below* for an example).

Pineda (1999) observed horizontal and vertical larval distribution in internal-bore warm fronts (i.e., buoyant gravity currents). In Southern California, nearshore internal tidal bores occur in two phases. First, a deep, cold-water mass is advected shoreward, displacing warm surface water offshore and creating a pressure imbalance between heavier inshore water and lighter offshore water. A surface front may or may not form between the inshore cold water and the offshore warm water (*see* fig. 7 with a surface front and fig. 8 without a front in Pineda 1999). In the second phase, cold water recedes offshore and a “warm” internal bore, or surge, returns, and can propagate all the way to the shore. Only *Chthamalus* spp. and *Pollicipes polymerus* barnacle larvae accumulated at the propagating fronts, with no evidence of accumulation for bryozoan cyphonautes. The untested hypothesis to explain these results was that barnacle larvae would respond to the convergent downwelling currents at the front by swimming up, resulting in accumulation at the front. The cyphonautes would behave more as passive particles, with no swimming against the frontal downwelling currents and no accumulation. The results suggest that only

Acknowledgments

The National Science Foundation provided support for K.R.H. (OCE-9810599 and OCE-0095059) and J.P. (OCE-9986627 and OCE-0083976). Both authors acknowledge the generous support of the Rinehart Coastal Research Center of the Woods Hole Oceanographic Institution. This is Woods Hole Oceanographic Institution contribution 10818.

larvae that swim against the downwelling currents or that are sufficiently buoyant would be transported onshore, reach the adult habitat, and have an opportunity to complete their life cycle. The horizontal distribution of larvae across the fronts showed that the most abundant frontal larvae, the gooseneck barnacle *P. polymerus*, had a predominately offshore distribution. The offshore origin of the larvae suggested that the velocity of the currents u behind the front was faster than the speed of the front c . Observations of the current speed and the phase speed of the fronts showed that $u > c$ close to the sea surface in one out of three events. The time-averaged onshore currents increased toward the surface, but because the Doppler current meter did not resolve the currents near the surface (2 m and shallower), it is possible that u was underestimated. We also note that similar gravity current dynamics might also occur during the relaxation of an upwelling front after the cessation of wind forcing and prior to the arrest of the front by geostrophic adjustment.

Britter and Simpson (1978) and Simpson and Britter (1979) (*also see* Simpson 1997 and references therein) studied the case of a dense gravity current advancing over a horizontal surface, a no-slip condition. Their observations show, within the bulk of the dense fluid, $u > c$. This convergence of dense fluid toward the gravity current nose occurs because of the interfacial turbulent mixing and detrainment of light fluid in the region just behind the gravity current head. However, because of the no-slip boundary, it is unclear how these observations would compare to the internal tidal bore warm fronts, where the gravity current is in contact with the air, effectively a stress-free boundary. Furthermore, their point measurements at a fixed distance behind the gravity current nose did not fully resolve the structure of the flow near the nose, a region of critical importance for the accumulation and transport of larvae.

Here, we test the hypothesis that larvae and other particulate matter initially well behind the nose of the gravity current can be accumulated near the nose and then transported with the gravity current. We conducted several simple laboratory experiments using buoyant gravity currents generated by a dam release. Measurements of the two-dimensional flow structure in the neighborhood of the gravity current head are made using digital particle image velocimetry (DPIV) (Raffel et al. 1988). Results are shown for two cases: (1) the ambient fluid ahead of the front has uniform density and (2) the bore propagates into a fluid capped with a thin layer of water with the same density as the dammed fluid (a two-layer stratification). For the first case, we also present an experiment in which buoyant plastic particles were placed on the surface behind the front and their subsequent motion toward the front is observed. These experiments are supplemented by two-dimensional nonhydrostatic numerical modeling and analysis of Lagrangian particle advection to quantify aspects of larval accumulation and transport as a function of bore properties and particle buoyancy.

Laboratory experiments

The laboratory experiments were conducted to examine accumulation and transport of particles (e.g., larvae) by

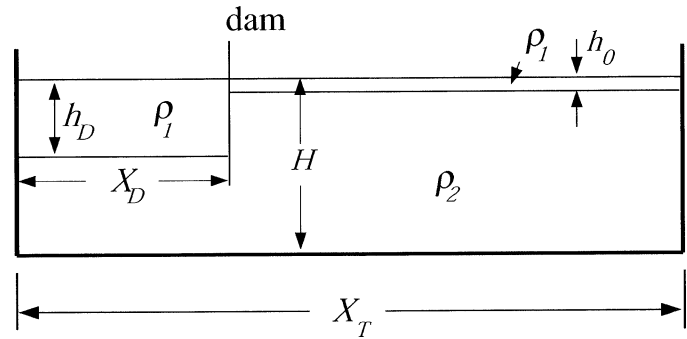


Fig. 1. A sketch of the experimental setup. The total water depth is H . The depth of the buoyant fluid upstream of the dam is h_D , and that downstream is h_0 . The upper layer has density ρ_1 and the lower denser layer has density ρ_2 . The tank has total length X_T , with the length of the dammed region X_D .

buoyant gravity currents. The goal of the experiments was not a thorough exploration of the relevant parameter space, but rather a clear demonstration of the process. The ability of gravity currents to accumulate particles was explored by observing the motion of buoyant particles on the free surface (experiment I) and by measurement of the two-dimensional (x - z) velocity field in the neighborhood of a gravity current head (experiment II). In the first case, the advection of particles initially well behind the gravity current nose toward the nose was observed in spite of the inhibiting effects of surface tension that are difficult to avoid at these laboratory scales. In the second experiment, the measured velocity fields indicate that only gravity currents (zero upstream buoyant fluid depth) will result in significant accumulation of particles at the nose. Undular bores, or surges, into a preexisting two-layer stratification might transport trapped parcels of fluid but do not lead to accumulation.

Experimental methods—Both types of experiments were conducted in tanks as sketched in Fig. 1. The tanks were first filled to a fixed depth (slightly less than total water depth, H) with filtered seawater with density ρ_2 . A vertical Plexiglas panel, which spanned the width of the tank, formed the dam and was sealed with silicon vacuum grease to prevent leaks. Fresher water of density ρ_1 was slowly introduced via floating sponge diffusers to form a layer of depth h_D behind the dam. The interface between the layers remained thin, on an order of 1.5 cm. In some cases, the dam was not put in place until a thin buoyant layer of depth h_0 was present over the whole tank, resulting in a two-layered stratification downstream of the dam. The length of the tank is X_T , and that of the dammed fluid section is X_D . In experiment I, the tank has $X_T = 17$ m, and the length of the dammed region $X_D = 4$ m. The tank was 0.4 m wide and 0.6 m deep. Experiment II was conducted in a smaller tank with $X_T = 5.49$ m, $X_D = 1.5$ m, width = 0.23 m, and depth = 0.5 m. In both experiments, $\rho_2 \approx 1.02$ and $\rho_1 \approx 0.9982$ – 1.018 were determined with a Anton–Paar densitometer.

In experiment I, 4-mm-diameter nylon beads (density = 0.95 g cm^{-3}) were placed at the surface of the buoyant fluid (dyed blue for visualization) behind the dam. The dam was

removed and the motion of the beads relative to the gravity current nose was recorded with both top- and side-view video cameras placed on a carriage that was moved down the tank with the gravity current head.

In experiment II, the velocity field within the bore head region was determined at a location centered 1.5 m downstream of the dam. The buoyant fluid was seeded with pliolite particles (density 1.026 g cm^{-3} and diameter $100\text{--}200 \mu\text{m}$). A vertically oriented 1.5-cm-wide light sheet formed from halogen lamps was placed along the central axis of the tank. Side view images of the particle motion within the light sheet were obtained with a black and white progressive scan video camera (Pulnix model 9702) and directly digitized at 30 frames per second into a personal computer. The imaged area (typically 648×340 pixels) was about 30 cm in the along-tank direction (x) and extended about 15 cm below the free surface.

The speed of the bore nose, c , through the imaging area was obtained by analyzing composite images of three to six sequential video frames from which the nose of the current could be easily identified by the structure of the resulting particle streaks. Five to six such composites separated in time could be used to determine the nose position $x_{\text{nose}}(t)$ across the image area from which c was determined by linear fit to the discrete x_{nose} versus t data. Horizontal, u , and vertical, w , velocities as functions of depth z and time t at the center of the image area, 1.5 m downstream of the dam, were determined using standard DPIV cross-correlation methods (Raffel et al. 1988). Velocities were determined from a pixel interrogation area of 32×32 pixels displaced vertically by 16 pixels, resulting in a velocity estimate about every 0.75 cm (at $21 \text{ pixels cm}^{-1}$). Vertical velocity data were typically very noisy because of the relatively small velocities (i.e., small vertical particle displacements). However, the ability of a gravity current to accumulate particles is determined principally by the horizontal velocity (the ratio u/c) which produced a robust signal in the cross-correlation for particle displacements.

Experimental results—The results of experiment I with buoyant surface particles is shown in Fig. 2, where $h_d = 14 \text{ cm}$, $h_0 = 0 \text{ cm}$, $H = 44.1 \text{ cm}$, $\rho_1 = 0.9982 \text{ g cm}^{-3}$, and $\rho_2 = 1.0220 \text{ g cm}^{-3}$. The three panels give side-view images at 3.5, 5.5, and 7.5 m downstream from the dam. The images show the buoyant gravity current fluid (dyed) in which the positions of buoyant beads are indicated by the thick lines above the free surface of each image. The particles are not easily seen in these still images because of their relatively small size (~ 2 pixels in the image) and parallax effects, but they are determined from the top-view images and side-view videos, where the motion of the particles makes them readily apparent. The marked particles were initially behind the dam and were identified in both the side-view and top-view video images as remaining near the center of the tank and thus avoiding sidewall influences. From panel a to c in Fig. 2, three of the five particles are swept toward the nose of the current. The other two remain near their positions in panel a. Attempts to quantify this behavior with other runs of experiment I were generally unsuccessful because of a variety of influences, including surface tension and sidewall friction

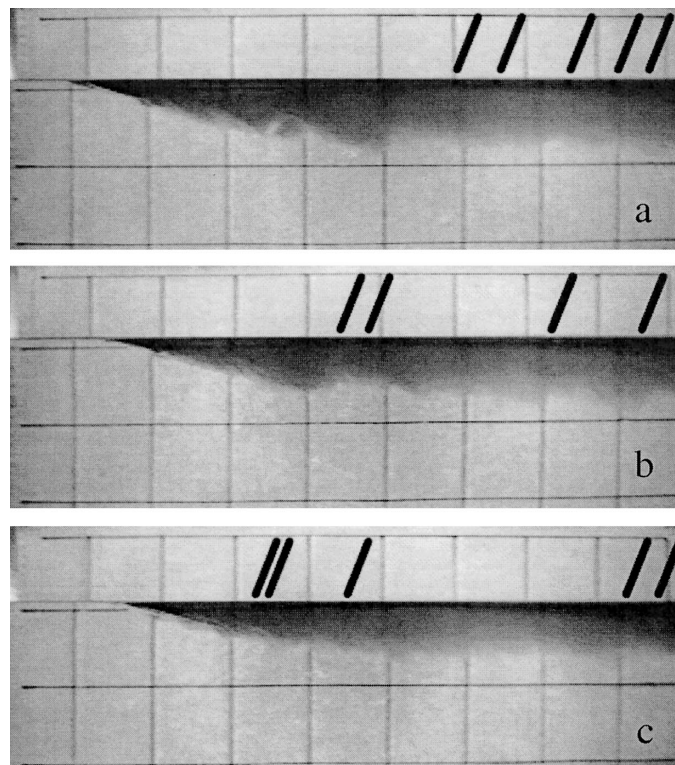


Fig. 2. Side-view images of a buoyant gravity current in experiment I for $h_d = 14 \text{ cm}$, $h_0 = 0 \text{ cm}$, $H = 44.1 \text{ cm}$, $\rho_1 = 0.9982 \text{ g cm}^{-3}$, and $\rho_2 = 1.0220 \text{ g cm}^{-3}$. The centers of each image are (a) 3.5, (b) 5.5, and (c) 7.5 m downstream of the dam, and the background grid has 10-cm spacing. The thick lines above the water surface indicate positions of buoyant particles, which are difficult to see in the images.

effects, which both act to inhibit, or slow, the rate of accumulation. Furthermore, the finite length of the tank also limited the duration of an experiment. However, the qualitative behavior of particle advection toward the nose of the gravity current shown in Fig. 2 was robust.

Quantitative information was obtained from the DPIV analysis of the horizontal velocity u in experiment II. Figure 3a shows the computed velocity vectors as a function of depth z and time t as a gravity current propagates past the interrogation region. In this run, $h_d = 17.5 \text{ cm}$, $h_0 = 0 \text{ cm}$, $H = 32.7 \text{ cm}$, $\rho_1 = 1.0169 \text{ g cm}^{-3}$, and $\rho_2 = 1.0201 \text{ g cm}^{-3}$. The time axis has been multiplied by the observed gravity current speed $c = 4.77 \text{ cm s}^{-1}$ to give an equivalent distance ct behind the bore nose ($ct = 0$). Figure 3b shows contours of the scaled horizontal velocity, u/c . There is a region of fluid near the surface, beginning about 10 cm behind the nose, with fluid velocities greater than the bore speed ($u/c > 1$). The maximum speeds are $u/c \approx 1.3$ and occur between 40 and 60 cm behind the nose. The average velocity near the surface ($z = -0.75 \text{ cm}$) in the $u/c > 1$ fluid is $u/c = 1.14$. The thick region of slower velocities, $0 < u/c < 1$, between $ct = 30\text{--}65 \text{ cm}$ is within the region of intense mixing and detrainment of buoyant fluid from the upper layer. Clearly, particles originating behind the bore nose will be

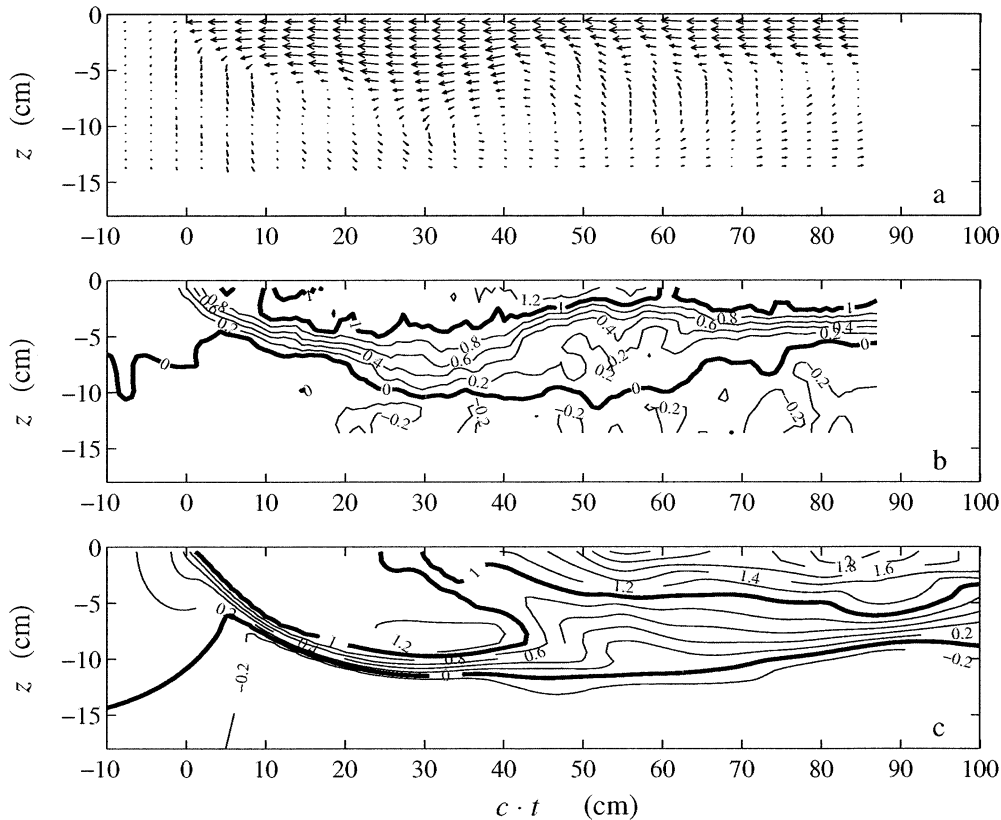


Fig. 3. (a) Experimentally determined velocity vectors for an experiment with $h_D = 17.5$ cm, $h_0 = 0$, $H = 32.7$ cm, $\rho_1 = 1.0169$ g cm $^{-3}$, and $\rho_2 = 1.0201$ g cm $^{-3}$. The vectors (arbitrarily scaled) are plotted as functions of depth z below the free surface ($z = 0$) and time t multiplied by the observed gravity current speed $c = 4.77$ cm s $^{-1}$ to give an equivalent distance behind the nose position ($ct = 0$). (b) Contours of horizontal velocity u , scaled by c , from panel a. (c) Contours of scaled horizontal velocity u/c from a numerical model set up with the parameters of the experiment in panels a and b. The numerical model gave $c = 4.62$ cm s $^{-1}$.

advected toward the front and, as will be demonstrated in the numerical modeling section below, will accumulate there if they are buoyant enough to avoid being swept down in the convergence region.

When the buoyant fluid behind the dam is released into an ambient fluid with two-layer stratification, the situation is quite different. In this case, the leading disturbance is an undular bore (e.g., Crook and Miller 1985) rather than the nose of a gravity current. Figure 4a,b shows the velocity vectors and the horizontal scaled velocity field u/c , respectively, for a case with $h_0 = 1$ cm. The other parameters ($h_D = 17.5$ cm, $H = 32.7$ cm, $\rho_1 = 1.0142$ g cm $^{-3}$, and $\rho_2 = 1.0177$ g cm $^{-3}$) are similar to the previous example in Fig. 3a,b. Now the horizontal velocity in the buoyant fluid is everywhere less than the nose speed $c = 5.39$ cm s $^{-1}$, except in a small region about $ct = 35$ – 55 cm behind the surge front. Fluid behind the leading edge of the intrusion does not flow toward the front in a frame moving with the intrusion, and accumulation will not occur. However, the patch of fluid with $u/c > 1$ is associated with a vortical motion centered at $(ct, z) = (32, -10$ cm) (Fig. 4a) that might be capable of transporting particles that are trapped initially within the vortex core.

Numerical modeling

The laboratory experiments indicate that gravity currents are capable of accumulating and transporting buoyant particles (or larvae that swim vertically in response to downwelling flows). Surges into an ambient two-layer stratification will not accumulate particles near the front but might transport particles within vortex cores. Further details of these flows, including Lagrangian particle motions, are investigated using a numerical model of the flow. The numerical modeling allows an exploration in more detail of a larger parameter space than could be easily undertaken in the laboratory. This is particularly so for the Lagrangian motion of buoyant particles in the flow. We accomplish this modeling using a two-dimensional (x, z) model of stratified flow set up to replicate the basic conditions of the experiments.

Numerical model—The numerical model is formulated to solve for two-dimensional incompressible motion in a density-stratified fluid. The *nondimensional* governing equations consist of the momentum equation,

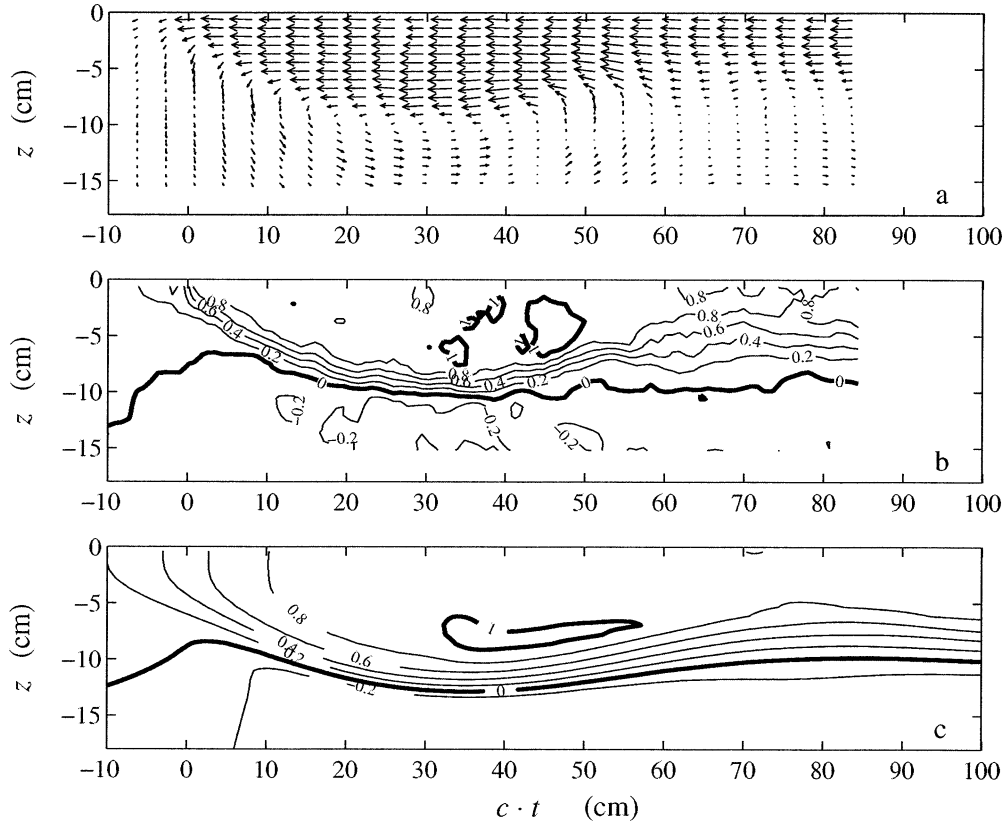


Fig. 4. (a) Experimentally determined velocity vectors for an experiment with $h_d = 17.5$ cm, $h_0 = 1$ cm, $H = 32.7$ cm, $\rho_1 = 1.0142$ g cm $^{-3}$, and $\rho_2 = 1.0177$ g cm $^{-3}$. The vectors (arbitrarily scaled) are plotted as functions of depth z below the free surface ($z = 0$) and time t multiplied by the observed gravity current speed $c = 5.39$ cm s $^{-1}$ to give an equivalent distance behind the nose position ($ct = 0$). (b) Contours of horizontal velocity u , scaled by c , from panel a. (c) Contours of scaled horizontal velocity u/c from a numerical model set up with the parameters of the experiment in panels a and b. The numerical model gave $c = 4.77$ cm s $^{-1}$.

$$\frac{\partial \mathbf{u}}{\partial t} + (\mathbf{u} \cdot \nabla) \mathbf{u} = -\nabla p - \mathbf{k}s + \nabla \cdot (\mathbf{K}_M \nabla \mathbf{u}) \quad (1)$$

the statement of incompressibility,

$$\nabla \cdot \mathbf{u} = 0 \quad (2)$$

and the mass conservation equation,

$$\frac{\partial s}{\partial t} + \mathbf{u} \cdot \nabla s = \nabla \cdot (\mathbf{K}_\rho \nabla s) \quad (3)$$

The equations employ the Boussinesq assumption, in which effects of density variations in momentum (Eq. 1) are significant only in the buoyancy term, $\mathbf{k}s$. The dynamic pressure is p , \mathbf{K}_M (\mathbf{K}_ρ) is the turbulent momentum (mass) diffusion coefficient, and t is time. Here, $\mathbf{u} = (u, w)$, where u is the horizontal (x) velocity and w is the vertical (z) velocity. In the scaled density difference,

$$s = \frac{\rho - \rho_0}{\Delta \rho}$$

ρ is the dimensional density, ρ_0 is a constant reference density, and $\Delta \rho = \rho_2 - \rho_1$ is the dimensional density difference between the layers. The unit vector in the z direction is \mathbf{k} ,

and ∇ is the two-dimensional gradient operator. Equations 1–3 have been nondimensionalized using the total depth H for (x, z) , $\sqrt{g'H}$ for \mathbf{u} , $\rho_0 g'H$ for p , and $\sqrt{H/g'}$ for t . The reduced gravity $g' = (\Delta \rho / \rho_0)g$. The mass and momentum diffusion coefficients were scaled by $\sqrt{g'H^3}$.

The subgrid model for the turbulent eddy viscosity \mathbf{K}_M follows the Smagorinsky (1963) model,

$$\mathbf{K}_M = \begin{cases} (C\Delta)^2 |D| (1 - \text{Ri})^{1/2}, & \text{for } \text{Ri} \leq 1 \\ 0, & \text{for } \text{Ri} > 1 \end{cases} \quad (4)$$

Here, C is a constant, and $\Delta = (\Delta x \Delta z)^{1/2}$ is a measure of the grid resolution. The total (nondimensional) fluid deformation is

$$D^2 = \frac{1}{2} \sum_{i=1,2} \sum_{j=1,2} \left(\frac{\partial u_i}{\partial x_j} + \frac{\partial u_j}{\partial x_i} \right)^2$$

where the subscripts refer to the x ($i, j = 1$) and z ($i, j = 2$) velocities and directions. The Richardson number is

$$\text{Ri} = \frac{-1}{D^2} \frac{\partial s}{\partial z}$$

The dynamical basis of this subgrid model is an assumption

of a quasisteady local turbulent kinetic energy balance and is discussed by Winters and Seim (2000). As in Winters and Seim, we use a typical value of $C = 0.17$ for all numerical runs. The turbulent Prandtl number $Pr = K_M/K_p$ is set to 1.

The model was solved in a rectangular domain with dam-break initial conditions (Fig. 1). The initial density distribution $s(x, z, t = 0)$ varied from $s = 0$ in the buoyant fluid to $s = 1$ in the dense region. The stratification had a $\tanh(\lambda z)$ shape with a nondimensional thickness $\lambda^{-1} = 30$, which for $H = 33$ cm is about 1 cm, comparable to the laboratory runs. The horizontal density jump at the dam was similarly smoothed, and the initial velocity field \mathbf{u} was 0. The model has a rigid lid, and the horizontal and vertical boundaries are impermeable with zero tangential stress (slip boundaries) and no flux for the density.

The numerical solution uses a cell-centered (\mathbf{u} and s) second-order fractional-step projection method (Bell and Marcus 1992). The model employs a second-order Godunov-type method for computing the nonlinear advection terms. This is advantageous in the gravity current problem, where sharp gradients are expected. The numerical grid had uniform grid spacing Δx and Δz . In all the runs presented here, we used 40 grid points in the vertical and square cells of $\Delta x = \Delta z = 0.025$. The numerical time step $\Delta t = 0.0025$.

The Lagrangian motion of particles in the fluid was calculated from

$$\frac{d\mathbf{x}_p}{dt} = \mathbf{u}(\mathbf{x}_p, t) + \mathbf{k}w_b \quad (5)$$

where $\mathbf{x}_p = (x_p, z_p)$ is the particle position, \mathbf{u} is the numerically calculated fluid velocity field, and w_b is a constant buoyancy velocity (nondimensionalized by $\sqrt{g'H}$). Equation 5 is integrated with a fourth-order Runge–Kutta method and bilinear interpolation in space and linear interpolation in time to determine $\mathbf{u}(\mathbf{x}_p, t)$ from \mathbf{u} on the numerical grid.

The two-dimensionality of the model is a compromise, and some aspects of the flow might not be very well represented. For example, in three dimensions, Kelvin–Helmholtz billows, which form in behind the gravity current head, are unstable to transverse perturbations and will break down. However, in a two-dimensional model, the billows would not break down and could continue to grow via the inverse cascade of two-dimensional turbulence. However, the subgrid mixing model will inhibit unrestrained growth of the billows. The relevance of the two-dimensional model is backed by recent numerical work by Härtel et al. (2000), comparing two-dimensional and three-dimensional calculations of the gravity currents. They show that a “two-dimensional model is able to capture essential features of the flow at the head,” including gravity current propagation speeds, flow, and density structure. Afanasyev and Peltier (1998) reached similar conclusions in their study of stratified flow over an isolated bump. Differences between their two- and three-dimensional simulations (with the subgrid model Eq. 4) appeared only after a distance away of several bump half-widths. Klemp et al. (1994) used a two-dimensional model and found good agreement with laboratory experiments for basic gravity current properties such as bore speed and height. Maxworthy et al. (2002) have recently compared laboratory experiments

of gravity currents into a uniformly stratified ambient fluid to two-dimensional numerical solutions with very good agreement.

Numerical results—The results of a numerical calculation set up identically to the experiment in Fig. 3a,b are shown in Fig. 3c. The horizontal velocity u scaled by the numerically determined gravity current speed $c = 4.62$ cm s⁻¹ as a function of z and t at a point 150 cm downstream from the dam is shown. This can be compared directly to the experimental results in Fig. 3b. The qualitative agreement is good, though there are quantitative differences. Chief among these are higher velocities near the surface in the numerical model. Maximum speeds of $u \approx 2c$ occur, compared to $u \approx 1.3c$ in the experiments. The gravity current, as defined by the u structure, is slightly thicker in the numerical model. The bore speeds c differ only slightly. The high velocities and the region of surface velocity $u < c$ near $ct = 24$ – 30 cm are transient features because of the “instantaneous” nature of this picture and the inherently turbulent flow in the nose region. As will be seen below, velocity fields averaged over a range of t give a continuous region of surface velocities $u > c$ with maximum $u \approx 1.5c$.

The equivalent numerical result for the laboratory experiment with $h_0 = 1$ cm (Fig. 4a,b) is shown in Fig. 4c. Again, the qualitative comparison is good. Both the experiment and numerical result show surface velocities $u/c < 1$ and a small patch of flow with $u/c > 1$ on the trailing face of the surge head. Here the velocity magnitudes are in better quantitative agreement with the experiment.

Although both of these comparisons suggest shortcomings of the numerical model in the fine details, they also show that the fundamental features are reproduced. Use of a three-dimensional model, and perhaps a different subgrid-scale mixing model, would undoubtedly improve the comparison. However, the results suggest that qualitative and quantitative understanding of the accumulation and transport of Lagrangian particles in gravity currents and undular bores will be obtained from further analysis with the two-dimensional numerical model.

Lagrangian particles—The transport of neutrally buoyant particles ($w_b = 0$) to the front of a gravity current head is illustrated in Fig. 5a–c. The initial condition (Fig. 5a) is a dammed region of buoyant fluid ($s = 0$) in which a random array of 1,000 red particles is placed between $x = 8$ – 9 behind the dam ($x = 10$). The nondimensional depth of the buoyant fluid behind the dam is $h_D = 0.535$ (equivalent to the experimental situation of $h_D = 17.5$ cm with $H = 32.7$ cm). Another random grid of blue particles is placed in front of the dam between $x = 11$ – 12 and $z = 0.465$ – 1 . Note that only part of the computational domain, $0 \leq x \leq 30$ and $0 \leq z \leq 1$, is shown. Figure 5b,c shows the particles at $t = 18$ and 36 , respectively. The contours show the density field s in increments of 0.2. Most of the particles behind the dam are swept toward the front by $t = 36$, whereas only a very few of the particles initially ahead of the front are entrained into this region, and most of these are within the turbulent billows slightly behind the head.

When the downstream ambient fluid has a two-layer strat-

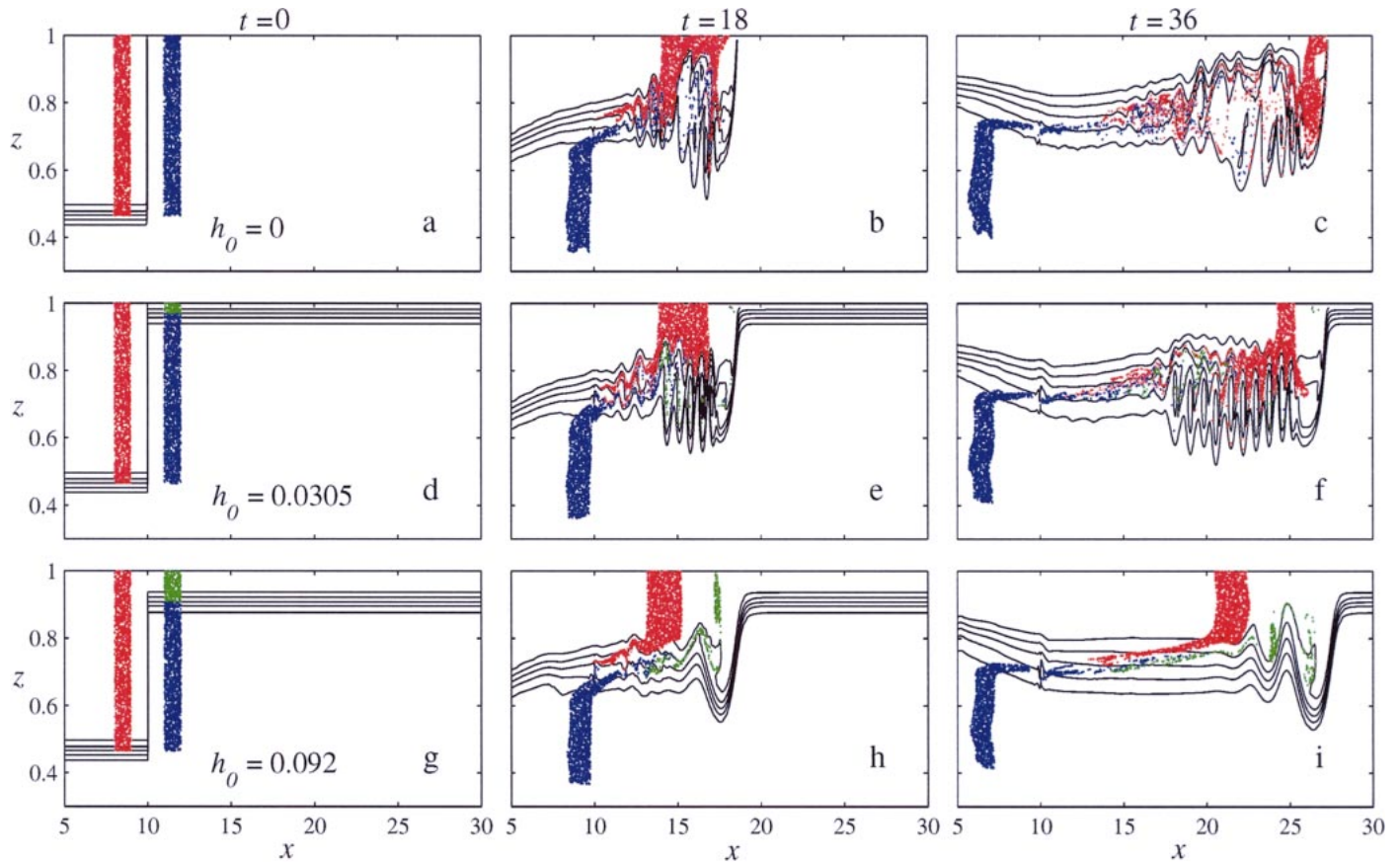


Fig. 5. Contours of the density field s (contour interval 0.2) and neutrally buoyant Lagrangian particles for runs with $h_0 = 0$ (panels a–c), $h_0 = 0.0305$ (panels d–f), and $h_0 = 0.092$ (panels g–i). In all cases $(h_D, X_D) = (0.535, 10)$. The solutions are shown for $t = 0$ (first column), $t = 18$ (second column), and $t = 36$ (third column). Note that only part of the computational domain ($0 \leq x \leq 30$ and $0 \leq z \leq 1$) is shown.

ification with $h_0 = 0.0305$ (Fig. 5d–f), the red particles are left behind, except for a thin tongue which is advected forward by a small region of overturning flow near the interface (Fig. 5f). Green particles placed in the upper layer in front of the dam are mostly left behind the undular bore front, and blue particles in the dense layer are again neither trapped nor transported within the front. The tendency for trapping and transporting some particles within a vortex core immediately behind the surge front (cf. Fig. 4) is clearer for a case with $h_0 = 0.092$ (Fig. 5g–i). In this example, a small fraction of the green particles initially in the upper layer in front of the dam are trapped in the overturning flow that forms the vortex (Fig. 5h) and is transported with the surge (Fig. 5i). Again, the red and blue particles are rapidly left behind the undular bore front. Figure 5d–f ($h_0 = 0.0305$) shows that there is some surface convergence of red particles just behind the leading wave. However, this convergent feature is moving backward relative to the leading edge of the disturbance. This does not occur for $h_0 = 0.092$ (Fig. 5g–i) and is a result of the more intense interfacial instabilities and mixing present for $h_0 = 0.0305$. It indicates that some surface accumulation can occur for small h_0 (>0) and that the transition between the strong accumulation for the gravity current case $h_0 = 0$ (Fig. 5a–c) and no accumulation at the front for larger h_0 (Fig. 5g–i) occurs over a small but finite

range of h_0 . This transition region should also be expected to depend on the precise structure of the stratification.

While particle transport can occur in the undular bore case, it is less efficient in comparison with the accumulation and transport in the case of the gravity current ($h_0 = 0$). This is directly associated with the presence, in the case of a gravity current, of large regions of the flow with $u > c$. In this case, particles that originate far behind the nose of the gravity current can be swept toward the nose to accumulate there and then be transported with the gravity current if they are retained at the nose. For $h_0 > 0$, only particles initially near the patch of recirculating flow (which includes the $u > c$ patch) can be transported with the bore. Other particles are left behind. However, we show below that in a gravity current, transport at the front over large distances will not occur for neutrally buoyant particles. A patch of neutrally buoyant particles would be advected to the front, but over a long enough time, the particles would all be swept down by the convergent flow near the nose and eventually left behind as they are detrained into the mixing region behind the bore head. Buoyancy (and/or behavior in the case of larvae) is necessary for particles to remain at the front once they have been accumulated there by the flow.

This aspect of the problem is examined using Lagrangian particle advection near the head of steady gravity currents.

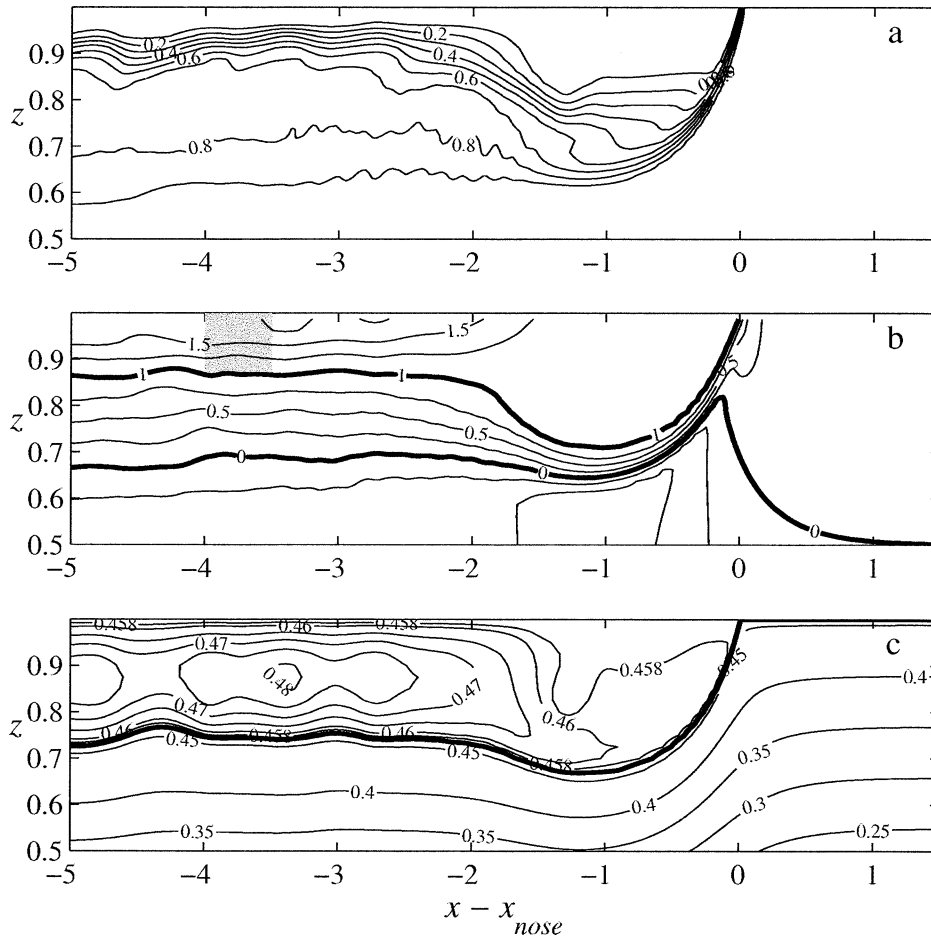


Fig. 6. The average bore head structure for a run with $(h_D, h_0, X_D) = (0.535, 0, 10)$. Contours of (a) s , (b) u/c , and (c) ψ . The gray box indicates the particle release area.

A steady gravity current was obtained by averaging the density, velocity, and streamfunction fields in the neighborhood of the gravity current nose, which was produced by a dam-break run (similar to Fig. 5a–c) but in a longer domain in order to avoid end-wall effects. The averaging in the three cases considered ($h_D = 0.25, 0.535$, and 0.75) was done between $t = 30$ – 40 (from model output at intervals of 0.5 time units) after the flow near the bore head had reached a quasi-steady state. The average fields were referenced to a coordinate system centered at the position of the nose $x_{\text{nose}}(t)$. As mentioned earlier, this averaging reduces the maximum horizontal velocities and smoothes the density field immediately behind the gravity current head in the region of Kelvin–Helmholtz billows.

The mean s , u/c , and streamfunction (ψ) fields in the ref-

erence frame moving with the gravity current speed c are shown for the central case $h_D = 0.535$ in Fig. 6. The results for $h_D = 0.25$ and 0.75 are qualitatively similar. The goal here is not a detailed study of the properties of the gravity currents themselves. However, to ensure that the numerical model is producing reasonable results, we include in Table 1 a summary of the results for the bore speed c and the thickness of the gravity current behind the bore head h_b , defined as in Klemp et al. (1994) as the depth from the upper surface down to the streamline $\psi = c$ (heavy line in Fig. 6c) at $x - x_{\text{nose}} = -3.5$. These numerical results for the scaled speed $c/\sqrt{h_D}$ as a function of h_D fall just above the experimental values from Rottman and Simpson (1983) and slightly below the numerical results of Klemp et al. (1994, see their fig. 10a). The scaled bore heights h_b/h_D versus h_D fall slightly above the Klemp et al. (1994, see their fig. 10b) results. The overall agreement is quite good, and differences likely are due to the averaging and differences in the numerical models (e.g., resolution).

The accumulation of particles within the bore head was examined by releasing 1,000 randomly placed particles between $x - x_{\text{nose}} = -4$ and -3.5 and in z above the mean position of the $u/c = 1$ contour (within the fluid approaching the nose). The thickness of this layer, h_c , is also listed in

Table 1. Buoyant fluid depth behind the dam h_D and results (nondimensional) for the average bore head conditions.

h_D	c	$c/\sqrt{h_D}$	h_b	h_c	\bar{u}_c	A	τ
0.25	0.334	0.670	0.093	0.054	0.421	0.274	59.2
0.535	0.456	0.623	0.259	0.133	0.673	0.650	22.5
0.75	0.476	0.550	0.292	0.213	0.577	0.891	41.3

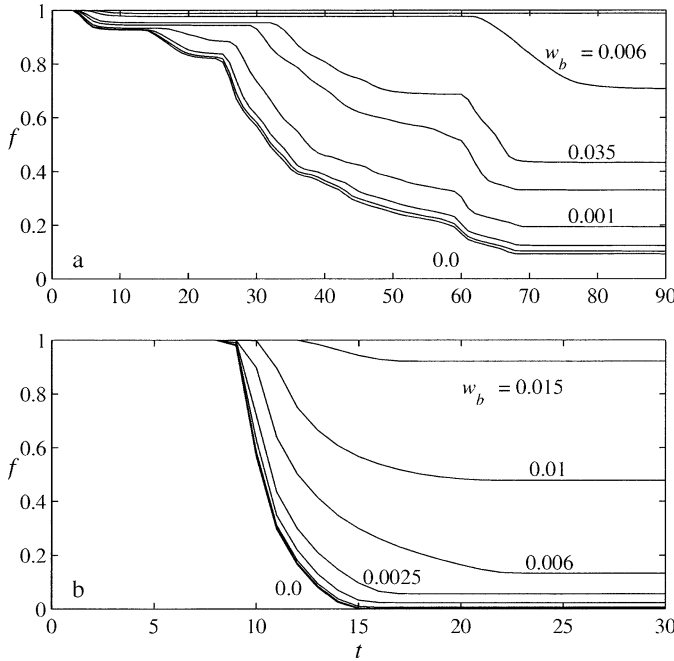


Fig. 7. The particle retention fraction f versus t for several indicated values of w_b in the range $w_b = 0-0.1$ for particles released behind the nose and $w_b = 0-0.05$ for particles released ahead of the nose. The calculations are based on the gravity current in Fig. 6 ($h_D = 0.535$). (a) Particles released behind the gravity current nose. (b) Particles released ahead of the gravity current nose.

Table 1. The particle release region for $h_D = 0.535$ is indicated by the gray box in Fig. 6b. An identical box (not shown) of 1,000 particles was also placed ahead of the nose between $x - x_{\text{nose}} = 1-1.5$. The particles were all given a constant buoyancy velocity w_b , and their positions were integrated in time with Eq. 5. If a particle position was $x_p < -4$, it was considered left behind the front and removed from the calculation.

Particle accumulation within the bore head region was quantified by computing the retention fraction as a function of time, $f(t)$, defined as the fraction of the initial 1,000 particles with positions $x_p > -4$. The results for particles released behind the gravity current nose for the case $h_D = 0.535$ (cf. Fig. 6) are shown in Fig. 7a for several values of w_b . In all cases, f reached a constant value by $t \approx 70-80$, which is termed the asymptotic, or steady state, retention fraction f_∞ . The result $f_\infty > 0$ for $w_b = 0$, where we would expect all particles to flow through the gravity current head and eventually be left behind, is the consequence of some particles having initial positions within a region of closed streamlines (see Fig. 6c) in which they must remain. The rate of decrease of f increases with decreasing w_b , and f_∞ increases with w_b . The particles retained in the nose all accumulate at the nose stagnation point $(x - x_{\text{nose}}, z) = (0, 1)$. For particles released ahead of the nose (Fig. 7b), f decreases more rapidly than those released behind the nose because of the rapid advection of particles underneath and then behind the gravity current nose region. Larger w_b are required for the same f_∞ when compared to the particles released behind the nose. Only for larger w_b are these particles able to rise

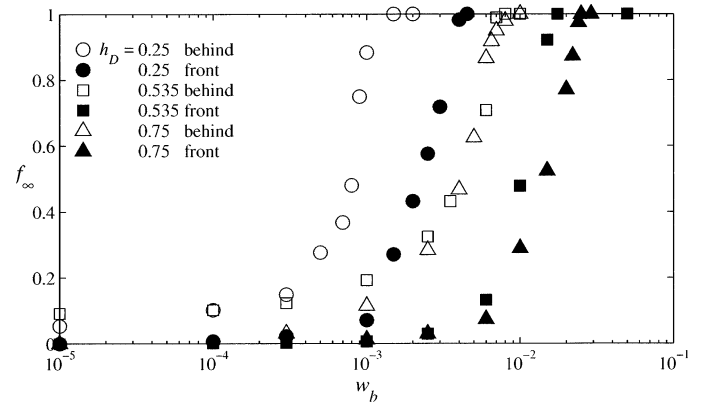


Fig. 8. The steady state retention fraction f_∞ versus w_b for $h_D = 0.25, 0.535,$ and 0.75 and for particles released both ahead of and behind the gravity current nose.

up into the upper layer and accumulate at the stagnation point before being swept out of the domain. The results for the two other cases, $h_D = 0.25$ and 0.75 , are qualitatively similar.

The use of steady, average velocity fields eliminates the possibility of turbulent fluctuations contributing to the motion of the particles and hence to the retention fraction. To address this issue, some calculations incorporating a stochastic, normally distributed displacement of the particles proportional to $K_M^{1/2}$ were undertaken. This first-order stochastic advection model is equivalent to an advection-diffusion model (Griffa 1996). Ultimately this leads to zero retention as $t \rightarrow \infty$ for any w_b . Particles are continually displaced from the nose stagnation point region and eventually will be lost by advection out of the domain ($x_p < -4$). This does, however, occur on a longer timescale than the development of the asymptotic states in Fig. 7. Ensemble averages of stochastic runs over the timescales in Fig. 7 are not very different from those shown. It is worth noting that random horizontal particle motions from, for example, larvae swimming capability would have much the same effect as the turbulent diffusion discussed here. Given the uncertainty in the subgrid model for K_M , it was decided to focus on the pure advection results to gain some insight into the accumulation and transport properties of gravity currents. Turbulence and three-dimensional effects will blur the final numbers, though the qualitative picture should remain.

The final value of the retention fraction f_∞ versus w_b is plotted in Fig. 8 for all three gravity currents ($h_D = 0.25, 0.535,$ and 0.75). In all three cases, f_∞ rapidly drops to < 1 once w_b decreases below a critical value of the buoyant velocity, w_b^* . Interestingly, particles released behind the bores for $h_D = 0.535$ and 0.75 both have $w_b^* \approx 0.009$, whereas for $h_D = 0.25$, $w_b^* \approx 0.0015$. However, this behavior is readily understood. The residence time for fluid parcels within the bore head ($-3.5 < x - x_{\text{nose}} < 0$) is τ ,

$$\tau = \frac{A}{(\bar{u}_c - c)h_c}$$

Here, A is the area of the gravity current head with $u \geq c$ for $-3.5 < x - x_{\text{nose}} < 0$ and

$$\bar{u}_c = \frac{1}{h_c} \int_{1-h_c}^1 u(z) dz$$

is the mean velocity over the depths where $u > c$ at $x - x_{\text{nose}} = -3.5$. Thus $(\bar{u}_c - c)h_c$ is the volume flux (per unit width) of buoyant fluid approaching the gravity current head. The time for a buoyant particle to rise a distance of h_c , the depth of the initial patch of particles, is h_c/w_b . Thus, the critical value w_b^* should scale as

$$w_b^* \sim \frac{h_c}{\tau} = \frac{h_c^2(\bar{u}_c - c)}{A} \quad (6)$$

The proportionality constant can be determined from the numerical results. (Values of \bar{u}_c , A , and τ for the three runs are listed in Table 1.) These give $w_b^*\tau/h_c = 1.64, 1.52$, and 1.74 for $h_D = 0.25, 0.535$, and 0.75 , respectively. Thus, for $w_b > w_b^* \approx 1.6h_c^2(\bar{u}_c - c)/A$ particles released behind the gravity current nose will be efficiently accumulated within the gravity current nose and ultimately transported with the propagating front.

A similar argument can be made for those particles released ahead of the gravity current. The appropriate time-scale is now the time for a particle to be advected from the release box (between $x - x_{\text{nose}} = 1-1.5$) to the end of the domain at $x - x_{\text{nose}} = -4$,

$$\tau \approx 5.5/c$$

The maximum distance a particle must rise is $h_c + h_b$, giving

$$w_b^* \sim \frac{(h_c + h_b)}{\tau} \sim (h_c + h_b)c \quad (7)$$

From Fig. 8, the values of w_b^* for particles released ahead of the bore are $w_b^* = 0.0045, 0.018$, and 0.025 for $h_D = 0.25, 0.535$, and 0.75 , respectively. The ratio $w_b^*/(h_c + h_b)c = 0.091, 0.101$, and 0.104 , respectively, giving $w_b^* \approx 0.1(h_c + h_b)c$.

To give some feeling for these results, consider the case of a gravity current in $H = 30$ m of water. The density jump across the front is taken to be due entirely to a temperature change of 4°C , which gives $g' = 0.01$ m s $^{-2}$ and $\sqrt{g'H} = 0.55$ m s $^{-1}$. Thus, for particles originating behind a gravity current head with $h_D = 0.535$, Eq. 6 gives the *dimensional* critical buoyancy velocity for complete trapping $w_b^* \approx 0.009\sqrt{g'H} \approx 5 \times 10^{-3}$ m s $^{-1}$. For $h_D = 0.25$ and 0.75 , $w_b^* \approx 0.1$ and 0.5 cm s $^{-1}$, respectively. Similarly, for particles released ahead of the gravity current, Eq. 7 gives the dimensional values $w_b^* \approx 0.3, 1$, and 1.4 cm s $^{-1}$ for $h_D = 0.25, 0.535$, and 0.75 , respectively. Particles originating ahead of the gravity current must have buoyancy velocities two to four times greater than those originating behind for efficient accumulation at the nose.

Discussion

These laboratory and numerical results show that near-surface horizontal particle velocities u in the light fluid of a buoyant gravity current are greater than the gravity current propagation speed c . Thus, in a frame moving with the gravity current, particles in the light fluid that originate behind

the gravity current nose will be advected toward the nose region where they can accumulate and be transported at speed c . In contrast, buoyant intrusions into a fluid with a preexisting buoyant fluid layer ($h_0 > 0$) were shown to contain regions of $u > c$ that are part of localized recirculation zones. However, these were isolated from the trailing currents (where $u < c$). In this situation, particles trapped in these regions can be transported with the phase speed c , but there will be no accumulation at the head of the intrusion of particles that originate behind the nose. This situation is similar to flow in large-amplitude internal solitary waves with trapped vortex cores (e.g., Derzho and Grimshaw 1997; Lamb 2002). Indeed, the evolution of the intrusion for $h_0 > 0$ will result in an undular bore, which asymptotically will lead to a train of solitary-like waves. These two cases illustrate a fundamental distinction between particle transport in gravity currents and waves (in which the undular bore represents the large-amplitude limit). These two situations occur in warm-water internal-bore fronts, where sometimes there is a surface density front, but on occasions there is a shallow layer of light water ahead of the surge (Pineda 1999).

Several authors describe the transport and accumulation of larvae and phytoplankton in propagating convergences (Shanks 1983; Farrell et al. 1991; Pineda 1994, 1999; Franks 1997; Shanks et al. 2000), but there is some confusion distinguishing transport and accumulation (e.g., Franks 1997; Pineda 1999), and the physical processes responsible for the accumulation have not been accurately and quantitatively documented. Although some mechanisms might transport and accumulate particles, others might only transport them. Features that accumulate and transport particles are likely much more efficient means of particle transport than those that only transport. Lamb (1997) shows that planktonic larvae undergo a finite displacement by the passage of nonlinear internal solitary waves and that, when aided by swimming or wind drift in the direction of wave propagation, particles can be transported with the wave phase speed. However, this appears to be an inefficient mechanism in comparison to buoyant gravity currents. The only caveat is if the internal solitary waves occur in packets of many waves, then the net transport distance can be substantial, but with a mean particle speed less than the wave phase speed. Still, particles that originate behind the wave (or packet) will not be transported. Similarly, transport occurs in internal solitary waves with trapped cores (Derzho and Grimshaw 1997; Lamb 2002), but there will be no accumulation. Furthermore, buoyant particles can rise out of the vortex core region and be left behind the wave.

The condition $u > c$ in warm-water surface-trapped fronts has been observed in the ocean (Pineda 1999; Shanks et al. 2000). The velocity u should be measured in the direction of front propagation c , determined from a temperature antenna array. This is important because in oceanic conditions, onshore moving fronts are not constrained to travel exactly parallel to the coastline. Pineda (1999) observed fronts that deviated from normal incidence by up to 31° . Lack of accurate estimation of the direction of front propagation could yield inaccurate u/c estimates.

The numerical calculations demonstrate that the efficient accumulation and transport of particles in gravity currents

depends on the behavior, or buoyancy, of the particles. Only sufficiently buoyant particles or larvae, which respond to downwelling flow by swimming upward, that originate in the buoyant fluid will be efficiently accumulated at the nose of a gravity current. The necessary vertical buoyancy velocity w_b for efficient accumulation can be estimated from a simple scaling analysis involving the particle residence time in the bore head region τ and the depth h_c of the $u = c$ velocity contour. Particles that originate in the dense fluid in front of the gravity current are not accumulated at the front unless they have significantly larger buoyancy or vertical swimming velocities than those particles that originate in the buoyant fluid. These results give rise to preferential trapping at the gravity current front of larvae that originate in the buoyant water behind the nose if the buoyancy, or swimming velocities, of all the larvae are equal. However, quantitative laboratory and field studies of vertical swimming behavior are lacking, with swimming speeds in stationary flows reported for only a few taxa (e.g., Yule 1982; Chia et al. 1984). These speeds range from $<0.1 \text{ cm s}^{-1}$ to $>5 \text{ cm s}^{-1}$ and fall above and below the dimensional w_b^* discussed at the end of the previous section. Invertebrate larvae and other plankton have characteristic distributions across the fronts, and these taxa might have different behaviors or buoyancy (Pineda 1999; Shanks et al. 2000). The transport and accumulation of these larvae would therefore depend on the behavior of the larvae and their cross-front distribution. Most invertebrate larvae are inefficient “ciliar” swimmers (Chia et al. 1984), with restricted capability for swimming against the downwelling currents. For these larvae, transport by these features would be more efficient if their original distribution is predominantly offshore. However, for buoyant particles and “muscular” plankton swimmers equally and uniformly distributed across the front, more particles would be collected from ahead of the front than from behind it simply because $c > \bar{u}_c - c$ (e.g., Pineda 1999). Franks (1997) modeled the accumulation of dinoflagellates in propagating internal-bore warm fronts, assuming that accumulated frontal cells originated ahead of the front, though his model did not allow for $u > c$. The results obtained here, however, suggest that the origin of the dinoflagellates could be behind the front.

This work was largely motivated by the observations of internal-bore warm fronts or surges, a phenomenon with diurnal/semidiurnal periodicity forced by the tides, and larval transport along the southern California coast (Pineda 1999). Also, nearshore time series of the rate at which planktonic larvae take up permanent contact with the substrate, the settlement rate, a proxy variable for nearshore larval abundance, are often dominated by peaks (Hawkins and Hartnoll 1982), suggesting the rapid arrival of large numbers of larvae. Shanks (1986) and Pineda (1991) also observed peaks in larval settlement. Shanks (1986) hypothesized that the settlement peaks were associated with internal wave arrival. Hawkins and Hartnoll's (1982) observations did indicate a correlation of high settlement with onshore wind but did not explain the mechanism. One explanation of settlement peaks not necessarily correlated with the wind or internal waves (where $u < c$) is gravity current fronts loaded with accumulated larvae that collide with the shore (Pineda 1994). The

implied concentrations of larvae during these settlement events is much larger than the offshore background concentration; thus, these observations are consistent with a shoaling of a propagating warm front in which particle accumulation has taken place. It is worth noting that the processes described here might also apply whenever lighter surface waters move over denser bottom waters as a gravity current. This situation might arise during relaxation of wind-driven upwelling (Farrell et al. 1991), in estuarine fronts, with atmospheric cooling of nearshore waters, and possibly as the result of cross-shore differential mixing.

References

- AFANASYEV, Y. D., AND W. R. PELTIER. 1998. The three-dimensionalization of stratified flow over a two-dimensional ridge. *J. Atmos. Sci.* **55**: 19–39.
- BELL, J. B., AND D. L. MARCUS. 1992. A second-order projection method for variable-density flows. *J. Comp. Phys.* **101**: 334–348.
- BRITTER, R. E., AND J. E. SIMPSON. 1978. Experiments on the dynamics of a gravity current head. *J. Fluid Mech.* **88**: 223–240.
- CHIA, F. S., J. BUCKLAND-NICKS, AND C. M. YOUNG. 1984. Locomotion of marine invertebrate larvae: A review. *Can. J. Zool.* **62**: 1205–1222.
- CROOK, N. A., AND M. J. MILLER. 1985. A numerical and analytical study of atmospheric undular bores. *Q. J. R. Meteorol. Soc.* **111**: 225–242.
- DERZHO, O. G., AND R. GRIMSHAW. 1997. Solitary waves with a vortex core in a shallow layer of stratified fluid. *Phys. Fluids* **9**: 3378–3385.
- FARRELL, T. M., D. BRACHER, AND J. ROUGHGARDEN. 1991. Cross-shelf transport causes recruitment to intertidal populations in central California. *Limnol. Oceanogr.* **36**: 279–288.
- FRANKS, P. J. S. 1997. Spatial patterns in dense algal blooms. *Limnol. Oceanogr.* **42**: 1297–1305.
- GRIFFA, A. 1996. Applications of stochastic particle models to oceanographic problems, p. 114–140. *In* R. J. Adler, P. Muller, and R. B. Rozovskii [eds.], *Stochastic modeling in physical oceanography*. Birkhauser.
- HÄRTEL, C., E. MEIBURG, AND F. NECKER. 2000. Analysis and direct simulation of the flow at a gravity current head. Part 1. Flow topology and front speed for slip and no-slip boundaries. *J. Fluid Mech.* **418**: 189–212.
- HAWKINS, S. J., AND R. G. HARTNOLL. 1982. Settlement patterns of *Semibalanus balanoides* (L.) in the Isle of Man (1977–1981). *J. Exp. Mar. Biol. Ecol.* **62**: 271–283.
- KLEMP, J. B., R. ROTUNNO, AND W. C. SKAMAROCK. 1994. On the dynamics of gravity currents in a channel. *J. Fluid Mech.* **269**: 169–198.
- LAMB, K. 1997. Particle transport by nonbreaking, solitary internal waves. *J. Geophys. Res.* **102**: 18,641–18,660.
- . 2002. A numerical investigation of solitary internal waves with trapped cores formed via shoaling. *J. Fluid Mech.* **451**: 109–144.
- MAXWORTHY, T., J. LEILICH, J. E. SIMPSON, AND E. H. MEIBURG. 2002. The propagation of a gravity current into a linearly stratified fluid. *J. Fluid Mech.* **453**: 371–394.
- PINEDA, J. 1991. Predictable upwelling and the shoreward transport of planktonic larvae by internal tidal bores. *Science* **253**: 548–551.
- . 1994. Internal tidal bores in the nearshore: Warm-water fronts, seaward gravity currents and the onshore transport of neustonic larvae. *J. Mar. Res.* **52**: 427–458.

- . 1999. Circulation and larval distribution in internal tidal bore warm fronts. *Limnol. Oceanogr.* **44**: 1400–1414.
- RAFFEL, M., C. WILLERTS, AND J. KOMPENHANS. 1998. Particle image velocimetry. Springer.
- ROTTMAN, J. W., AND J. E. SIMPSON. 1983. Gravity currents produced by instantaneous releases of a heavy fluid in a rectangular channel. *J. Fluid Mech.* **135**: 95–110.
- SHANKS, A. L. 1983. Surface slicks associated with tidally forced internal waves may transport pelagic larvae of benthic invertebrates and fishes shoreward. *Mar. Ecol. Prog. Ser.* **13**: 311–315.
- . 1986. Tidal periodicity in the daily settlement of intertidal barnacle larvae and an hypothesized mechanism for the cross-shelf transport of cyprids. *Biol. Bull. (Woods Hole)* **170**: 429–440.
- , L. LARGIER, L. BRINK, J. BRUBAKER, AND R. HOOFF. 2000. Demonstration of the onshore transport of larval invertebrates by the shoreward movement of an upwelling front. *Limnol. Oceanogr.* **45**: 230–236.
- SIMPSON, J. E. 1997. Gravity currents in the environment and the laboratory, 2nd ed. Cambridge Univ. Press.
- , AND R. E. BRITTER. 1979. The dynamics of the head of a gravity current advancing over a horizontal surface. *J. Fluid Mech.* **94**: 477–495.
- SMAGORINSKY, J. 1963. General circulation experiments with the primitive equations. *Mon. Weather Rev.* **91**: 99–164.
- WINTERS, K. B., AND H. E. SEIM. 2000. The role of dissipation and mixing in exchange flow through a contracting channel. *J. Fluid Mech.* **407**: 265–290.
- YULE, A. B. 1982. The application of new techniques to the study of planktonic organisms. Ph.D. thesis, Univ. College of New South Wales.

Received: 21 June 2002

Amended: 12 February 2003

Accepted: 27 February 2003